Structure and hydrogenation properties of a HfNbTiVZr high-entropy alloy

Dennis Karlsson[a, *], Gustav Ek[a], Johan Cedervall[a], Claudia Zlotea[b], Kasper Trans Møller[c], Thomas Christian Hansen[d], Jozef Bednarčík[e], Mark Paskevicius[c], Magnus Helgerud Sørby[f], Torben René Jensen[c], Ulf Jansson[a], Martin Sahlberg[a]

[a] Department of Chemistry – Ångström Laboratory, Uppsala University, Box 523, SE-751 20 Uppsala, Sweden
[b] Université Paris Est, Institut de Chimie et des Matériaux Paris-Est (UMR7182), CNRS, UPEC, 2-8 rue Henri Dunant, F-94320 Thiais, France
[c] Center for Materials Crystallography, iNANO, and Department of Chemistry, Aarhus University, Langelandsgade 140, 8000 Aarhus, Denmark
[d] Institut Laue-Langevin, 71 Avenue des Martyrs, 38000 Grenoble, France
[e] Deutsches Elektronen-Synchrotron DESY, Photon Science, Hamburg, Germany
[f] Institute for Energy Technology, Physics Department, P.O. Box 40, NO-2027 Kjeller, Norway

*Corresponding author email dennis.karlsson@kemi.uu.se

Abstract

A high-entropy alloy (HEA) of HfNbTiVZr was synthesised using an arc furnace followed by ball milling. The hydrogen absorption mechanism was studied by *in-situ* X-ray diffraction at different temperatures and by *in-situ* and *ex-situ* neutron diffraction experiments. The body centered cubic (BCC) metal phase undergoes a phase transformation to a body centered tetragonal (BCT) hydride phase with hydrogen occupying both tetrahedral and octahedral interstitial sites in the structure. Hydrogen cycling of the alloy at 500 ºC is stable. The large lattice strain in the HEA seems favourable for absorption in both octahedral and tetrahedral sites. The alloying concept of HEA:s therefore have potential as hydrogen storage materials, due to favourable absorption in all interstitial sites within the structure.

1. Introduction

Lately the effect of global warming has been generally accepted and the interest of renewable resources is constantly increasing. Hydrogen would serve this purpose as an alternative fuel; however, storage is a challenging task. Hydrogen storage in alloys and intermetallic compounds, with high energy density, could become a safe and volume effective alternative [1]. Among metal hydrides, the AB_5 and AB_2 Laves phase compounds and certain body centered cubic (BCC) based alloys show high reactivity with hydrogen. However, there is a need for new materials, with higher hydrogen capacity and lower cost.

The concept of high-entropy alloys (HEAs) was originally demonstrated by Yeh et al. in 2004 [2]. This original concept is based on equimolar alloys of five or more elements where a solid solution with a simple BCC or face centered cubic (FCC) type structure is formed. The solid solution is assumed to be thermodynamically stabilized by a high entropy of mixing ΔS_{mix}. This is possible if the enthalpy of mixing ΔH_{mix} is low (usually -10 kJ/mol $< \Delta H_{mix} <$ 5 kJ/mol). However, it should be noted that the effect of entropy of mixing on the formation of HEAs has been questioned and it has been proposed that other factors such as kinetics may be important for the formation of these materials. Another important parameter is the lattice distortion. When many metals with large differences in atomic radii are mixed, the crystal lattice will be strained or distorted. Typically, the lattice distortion, δ, is defined as:

$$\delta = \sqrt{\sum_i c_i \cdot (1 - \frac{r_i}{\bar{r}})^2}$$

where c_i and r_i are the atomic fraction and the atomic radius, respectively, of element i, $\bar{r} = \sum_i c_i \cdot r_i$. Empirical studies have shown that a value of $\delta < 6.6$ % is necessary in order to form a complete solid solution. Distortions higher than this critical value may lead to the formation of intermetallic precipitations such as Laves phases [3, 4].

Since 2004 the interest of HEAs has increased rapidly due to their promising mechanical properties for structural applications. For example, Senkov et al. studied an MoNbTaVW alloy with outstanding mechanical properties at elevated temperatures, outperforming the conventional Ni-based superalloys [5]. George et al. reported an HEA of CoCrFeMnNi with remarkable tensile properties at cryogenic temperatures, explained by a twinning deformation mechanism [6]. Furthermore, a combination of hard and soft phases is a promising alloying pathway to achieve high strength and high ductility HEAs [7, 8]. HEAs have also interesting magnetic properties and potential as thermoelectric materials [9, 10]. Finally, the HEAs have also, to some extent, been studied as hydrogen storage materials [11-13], e.g. the HfNbTiVZr alloy with a BCC structure has been demonstrated to possess excellent hydrogen storage properties [14]. Specifically, it was shown that this alloy could be hydrogenated with a H/M ratio of at least 2.5 in a body centered tetragonal (BCT) hydride phase, which is much more than in any other transition metal hydride. This is only possible if hydrogen could occupy both tetrahedral and octahedral sites in the lattice. The studies

of mechanisms for hydride formation of HEAs are, however, rather limited and further research is needed to fully understand the reaction pathways.

The purpose of this study is to investigate the kinetics and mechanism of hydride formation of a HfNbTiVZr HEA. The temperature dependence and kinetics of the hydrogenation process is studied using *in-situ* synchrotron radiation powder X-ray diffraction (SR-PXD) combined with neutron diffraction experiments. The latter enables determination of the position of the hydrogen atoms in the HEA hydride. Finally, isothermal absorption measurements was used to determine the thermodynamic parameters for the hydrogenation reaction.

2. Experimental

As-cast HfNbTiVZr were prepared by arc-melting in an Ar (g) atmosphere purified by a Ti-getter using a water cooled Cu crucible. Ti (99.995% pure, Chempur), V (99.95% pure, MRC), Zr (99.8% pure, Chempur), Nb (99.8% pure, Cerac) and Hf (99.6% pure, Johnson Matthey, Materials and Technology U.K.) in equiatomic amounts were re-melted together and turned around five times to ensure homogeneity. The total yield was > 99.9 %. The chemical composition of the samples was confirmed by EDS analysis, with no traces of Cu from the crucible. The ingot was then crushed, pulverised (by ball milling) and sieved to < 50 μm particles prior to the hydrogenation experiments. The synthesis and hydrogenation is described in an earlier communication [14].

The SETARAM PCTPRO volumetric instrument was used for the pressure-composition-isotherm (PCT) measurements on the HfNbTiVZr in powder form, at different temperatures up to 10 bar of hydrogen. The equilibrium time for the PCT measurements was set to 10 h per isotherm point. The thermodynamics can then be deduced from knowledge of the equilibrium pressure at different temperatures using the van't Hoff equation.

Structural characterisation of HfNbTiVZr powder was performed by *ex-situ* X-ray diffraction (XRD) using CuKα radiation in a Bruker D8 Advance diffractometer equipped with a Lynx-eye XE position sensitive detector. *In-situ* synchrotron radiation powder X-ray diffraction (SR-PXD) characterisation was carried out at the P02.1 beamline at DESY in Hamburg, Germany. The wavelength was determined as 0.20717 Å by using a LaB_6 standard. A PerkinElmer XRD1621 detector and an exposure time of 5 s per diffraction pattern were used during the experiments. The sample cell consisted of a sapphire tube connected to a vacuum pump and a pressurised hydrogen gas source [15]. After evacuating (10^{-2} bar) the sample container a hydrogen gas pressure of 100 bar was applied. The samples were then heated and kept at elevated temperatures (300, 400, 500 and 600 ^{o}C) during the experiments, using a Kanthal wire, and recorded using a thermocouple inside the sapphire tube. Cycling was performed by alternating vacuum and 100 bar hydrogen gas at the different temperatures.

The Fit2d program was used for data reduction from 2D images to 1D diffraction patterns. [16] The integrated diffractograms were refined using the Rietveld method [17] in sequential mode via the program FullProf [18] and in single-scan mode with Topas version 5. Prior to the sequential Rietveld

refinement, one diffractogram containing only the HEA phase and one containing only the hydride phase were refined. In the sequential Rietveld refinement all parameters except the scale factors, correlated to the amount of the phases, were fixed.

In-situ neutron powder diffraction (NPD) was performed at the instrument D1B at Institute Laue-Langevin (ILL) in Grenoble, France. A pyrolytic graphite monochromator (reflection 002) was used, giving a wavelength of 2.52 Å. The sample was placed inside a steel tube (inside diameter of 6.2 mm) connected to a deuterium (D_2) flask and a vacuum pump, giving the possibility to measure D_2-pressure ranging from vacuum up to 50 bar. The sample was heated up to 500 °C at 50 bar D_2 while measuring continuously. Then the sample was pressure cycled 5 times at 500 °C and diffraction patterns were collected for each cycle. The patterns were then refined using the Rietveld method [17] implemented in FullProf [18]. *Ex-situ* NPD was performed at the PUS diffractometer at the JEEP II reactor at Institute for Energy Technology (IFE), Kjeller, Norway [19]. Neutrons with the wavelength 1.5539 Å were provided by a Ge(511) monochromator. The sample was contained in a cylindrical vanadium sample holder with 6 mm diameter. The diffracted neutrons were detected with two detector banks, each with 7 vertically stacked 3He position-sensitive detector tubes covering 20^o scattering angle. The 2θ range from 10 to 130^o was covered by moving each detector to three different positions.

The microstructure of the samples, prior and after hydrogenation, was studied using a Zeiss Merlin scanning electron microscope (SEM) equipped with a secondary electron (SE) detector and an energy dispersive X-ray spectrometer (EDS). The EDS analysis was obtained using an acceleration voltage of 10 kV and a current of 2.0 nA. An area of around 500 x 500 µm was analysed for 20 min. The investigated surface of the as-synthesised material was prepared by mechanical grinding using 220 grit SiC paper followed by polishing with a 3 µm diamond slurry. A final polishing step using a SiO_2/H_2O_2 mix was used to reveal the microstructure.

3. Results and discussion

3.1. Synthesis and microstructure

The as-synthesised HfNbTiVZr (δ = 5.8% assuming 8-fold coordination of all metal atoms) crystallises in a BCC structure, and the corresponding XRD pattern is shown in figure 1. The unit cell parameter was determined to be a = 3.3659(2) Å. A significant peak broadening (FWHM around 1000% higher in (110) HEA compared to $(\bar{2}10)$ in the Al_2O_3 standard at the same Q values) is observed in the diffraction profile due to internal strain in the material, some of which possibly

originates from the crushing and milling of the original ingot, introducing stresses and a smaller grain size.

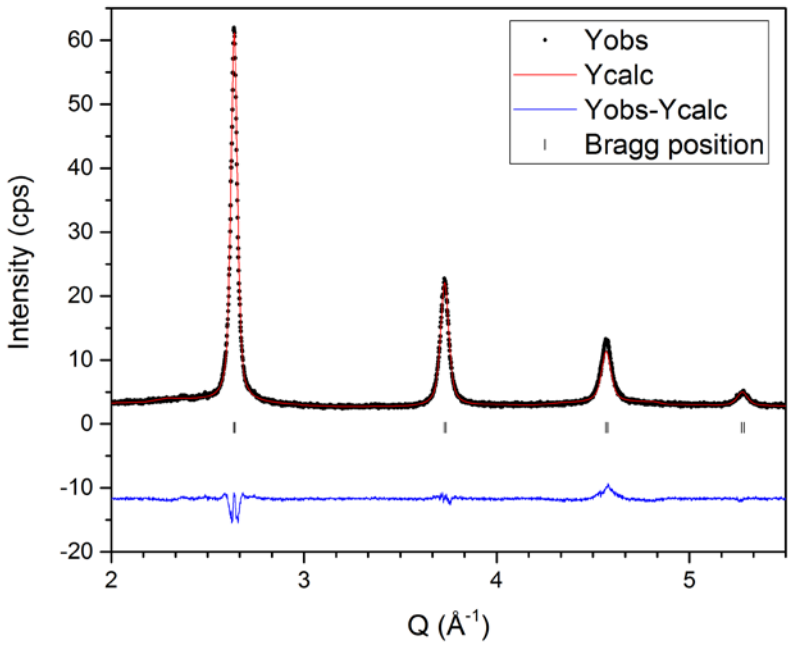

Figure 1. XRD pattern of the as-synthesised HfNbTiVZr. All peaks are explained by a BCC structure with a unit cell parameter of 3.3659(2) Å.

The microstructure and chemical distribution of the as-synthesised HEA can be seen in figure 2, is in agreement with an equimolar composition (see elemental composition in SI, table 1). The grain size is around 50 μm, which indicates that the peak broadening in the diffraction pattern in figure 1 cannot originate from a small grain size. From the EDS data (figure 2) it can be seen that all elements are homogeniously distributed in the different grains.

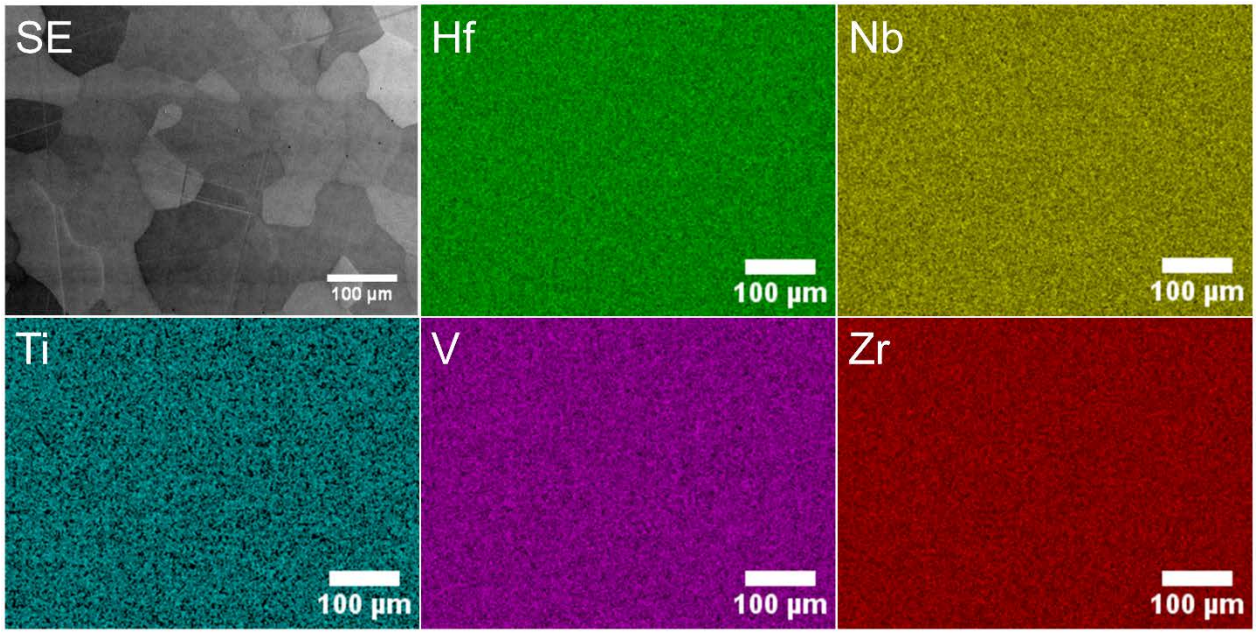

Figure 2. EDS maps of the as-synthesised HfNbTiVZr HEA. The elements are distributed homogenously in the grains. To the top left the SE image is shown.

SEM images of the as-synthesised HfNbTiVZr powder and the hydrogenated powder, figure 3, show a rather similar microstructure. The cracks induced from ball milling (figure 3 d), are assumed to provide transport possibilities for hydrogen, increasing the rate of hydrogen absorption. The as-milled powder can be seen in figure 3a and shows flake-like particles with a size around 50 µm. After hydrogenation the surface roughness decreases (figure 3 b) and smaller particles are observed in the powder. Figure 3 d-f show typical microstructure within the powder particles during one hydrogen cycle. Ball milling induces stresses in the material, which could favour crack formation when subjected to hydrogen, causing decrepitation of the powder. This has been studied in steel, where crack formation was observed in the residual stress field around an indent after subjecting the material to hydrogen, in agreement with higher hydrogen content due to lattice distortion in HEAs [20].

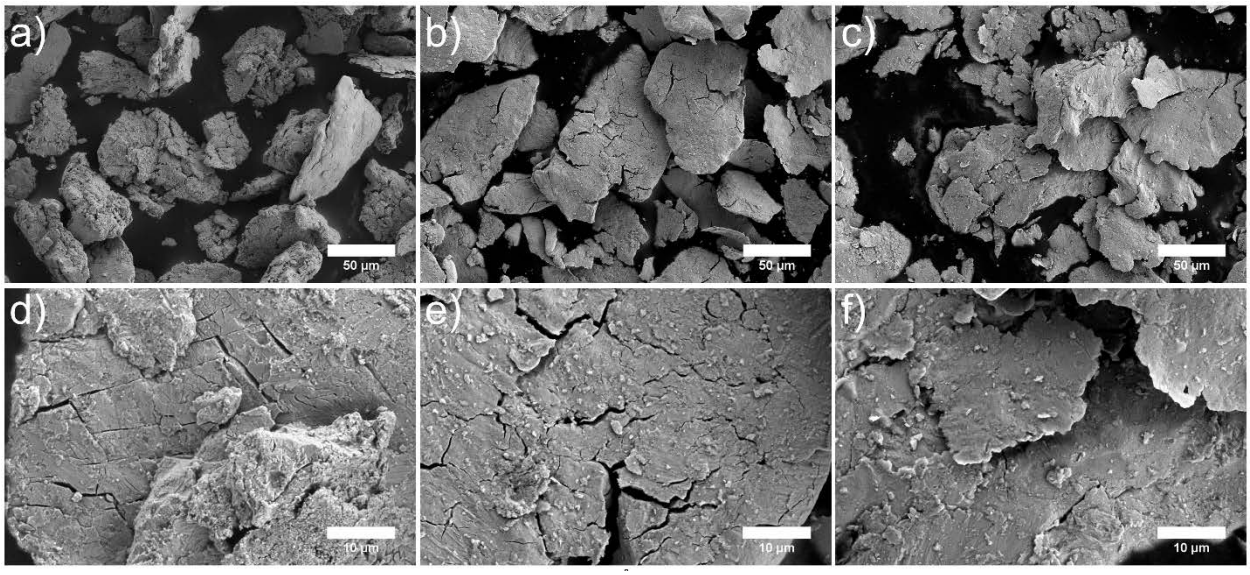

Figure 3. SEM InLens images of the as-synthesised HEA (a), the hydrogenated material (b) and the desorbed material (c). (d), (e) and (f) show typical microstructure at higher magnification for the as-synthesised HEA, the hydrogenated material and desorbed material, respectively.

3.2. *In-situ* X-ray diffraction measurements

Previously, a remarkably high hydrogen capacity was reported in the HfNbTiVZr high-entropy alloy, reaching up to 2.5 H/M [14]. It was suggested that the transformation during hydrogenation of the as-synthesised material can be described by a combination of the reaction mechanisms for many transition metal-hydrogen systems [21] and rare-earth metal-hydrogen systems [22]. To fully elucidate the reaction pathway during hydrogen absorption and desorption, *in-situ* SR-PXD experiments were performed at the Petra III synchrotron radiation facility in Hamburg, Germany [23]. As seen in figure 4, several cycling experiments at different temperatures were performed to map the HEA-H reaction pathways.

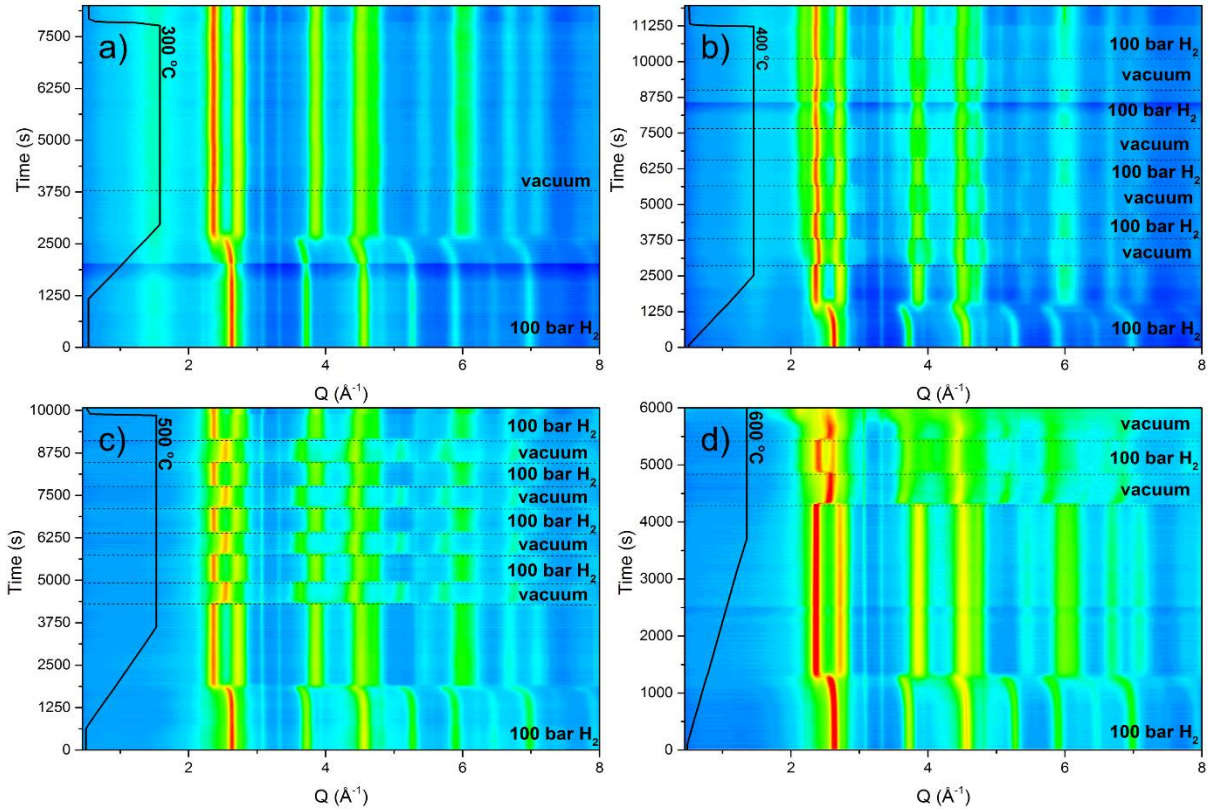

Figure 4. ***In-situ*** **SR-PXD of hydrogen cycling experiments at 300 ºC (a), 400 ºC (b), 500 ºC (c) and 600 ºC (d). The extra peaks in the diffraction data is WC contamination and intensity from the kanthal wire.**

As the temperature increases (as well as the hydrogen content in the alloy), a transition from the BCC-phase (α-phase) to a hydride phase (distorted FCC-lattice, β-phase) is observed just below 300 °C (figure 4a). The temperature was then kept at 300 °C while the hydrogen was evacuated and the system pumped down to vacuum. The hydride phase was observed to be stable under low vacuum (10^{-2} bar) and 300 °C, as no change can be seen in the diffraction profile. The hydrogenation reaction is initiated by a solid solution in the BCC-phase (α-phase) as seen by the large increase in the unit cell parameter (observed as a gradual shift in peak positions towards lower angles), see figure 5. The total volume expansion of the BCC unit cell is ~4 $Å^3$ (not corrected for thermal expansion), prior to the phase transition to the hydride phase.

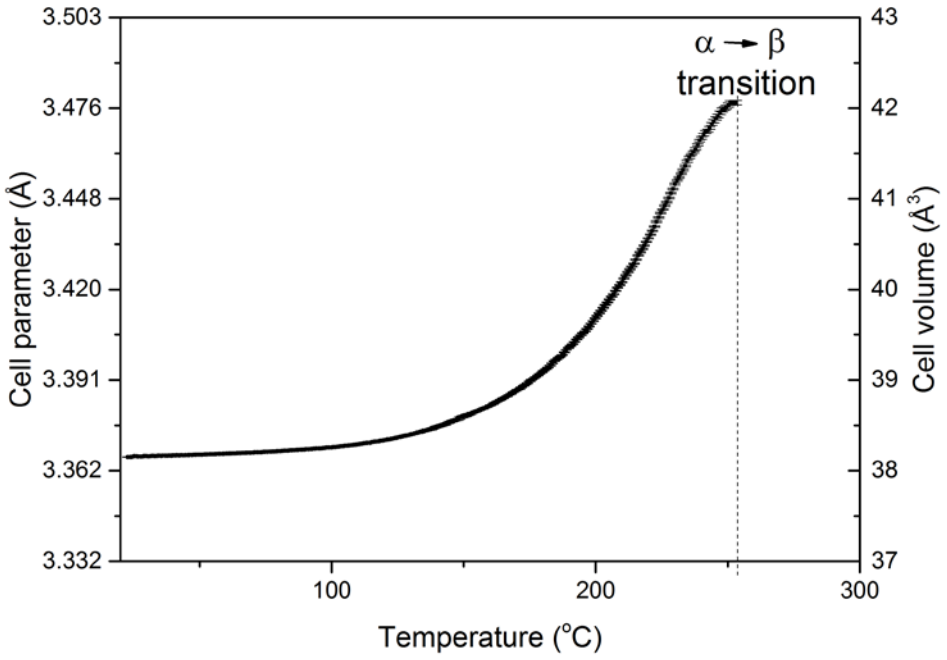

Figure 5. Increase of unit cell parameter *a* in the BCC phase prior to the phase transition. The volume expansion is related to a solid solution of hydrogen prior to the α-β-transition.

The distortion of the cubic structure can be seen as a change in the length of the *c*-axis, leading to a breakage of the cubic symmetry. The symmetry of the phase is then lowered from face centered cubic ($Fm\bar{3}m$) to body centered tetragonal (BCT, *I4/mmm*) as illustrated in figure 6. The different structures along the hydrogenation pathways were discussed previously [14], but different unit cell parameters were observed. In this study a decrease of the *c*-axis in the distorted FCC structure is observed, rather than an increase as described earlier. However, these results were obtained at elevated temperatures as compared to the room temperature data from ref. [14], which could explain the different behaviour.

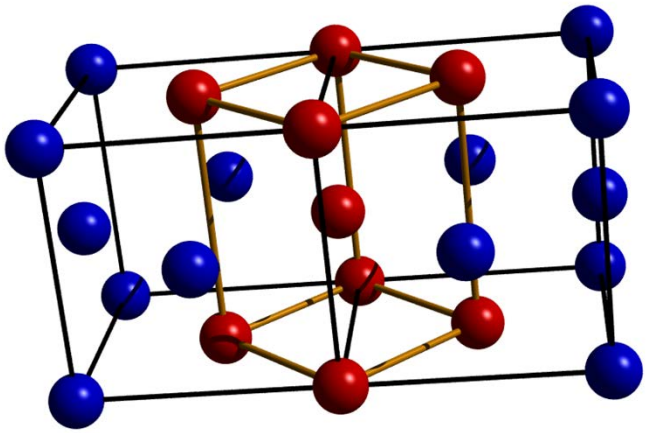

Figure 6. Breakage of the cubic symmetry as one of the cubic axes deviates from the ideal value. The black cells indicates the ideal FCC lattice, and the new tetragonal unit cell (*I4/mmm*) is marked in orange. The volume of the tetragonal unit cell is half of the cubic unit cell volume as $a_{tetra} * \sqrt{2} \cong a_{cubic}$.

Hydrogenation at 400 °C initially yields the same behaviour as at 300 °C. However, by exposing the hydride to vacuum at 400 °C, a change in the unit cell parameters of the BCT structure is observed, see figure 4b. The *c/a* ratio in the tetragonal unit cell is decreased from the nominal (at 100 bar H_2) 1.38 to 1.27 (1.414 corresponds to an undistorted FCC lattice). This change in unit cell parameters leads to a decrease of the unit cell volume from 48.9 $Å^3$ to 48.1 $Å^3$, which corresponds to a decrease in H/M by 0.3 assuming a volume increase of 2.9 $Å^3$ per hydrogen atom in the unit cell. The experimental value expected for a Laves phase hydride is 2.9 $Å^3$/H-atom, known as Peisls relationship [24] (but can be expected to be similar also in this case).

The continuous change of the *c/a* ratio during cycling can be seen as the material "breathing", where the unit cell volume increases with increasing hydrogen content in the material. Solid solubility in fluorite type hydrides (MH_{2+x}) is well known and is generally thought to originate from selective occupation of additional interstitial sites in the structure (octahedral *z*-site). [25] The site preference of hydrogen (deuterium) is described below based on NPD data.

Hydrogenation at 500 °C (100 bar H_2) yields a fully reversible transition from the BCC-alloy to a hydride phase (distorted FCC-lattice), figure 4c. By exposing the hydride to vacuum, hydrogen is desorbed and the material is transformed back to the initial BCC-structure. Furthermore, the material is stable under cycling, showing no trace of decomposition into other phases. However, the unit cell parameters change slightly during cycling, resulting in a reduced *c/a* ratio and an increase in unit cell volume from 48.7 to 49.6 $Å^3$ (table 1). This corresponds to an increase in H/M by 0.3 and suggests that either not all hydrogen is desorbed or that the material gets activated during cycling. At 600 °C (figure 4d), the material starts to decompose after the first absorption-desorption cycle and the measurement was ended after two cycles.

Table 1. Unit cell parameters for the hydride phase during cycling at 500 ºC.

Cycle	*a* (Å)	*c* (Å)	*c/a*	V (Å^3)
1	3.279(1)	4.531(1)	1.382	48.71
2	3.303(1)	4.516(2)	1.367	49.26
3	3.315(2)	4.501(3)	1.358	49.46
4	3.316(2)	4.503(3)	1.358	49.51
5	3.321(2)	4.494(3)	1.353	49.56

Figure 7 shows the Rietveld refinement of the hydride phase after one cycle at 500 ºC. The asymmetry of the (110) peak in the FCC lattice is explained by, the former discussed, lattice distortion to a BCT structure, which explains all the peaks from the sample. Rietveld refinements of extracted diffractograms (figure 8) at different temperatures showed the same *c/a* ratios for all temperatures, with very similar unit cell parameters.

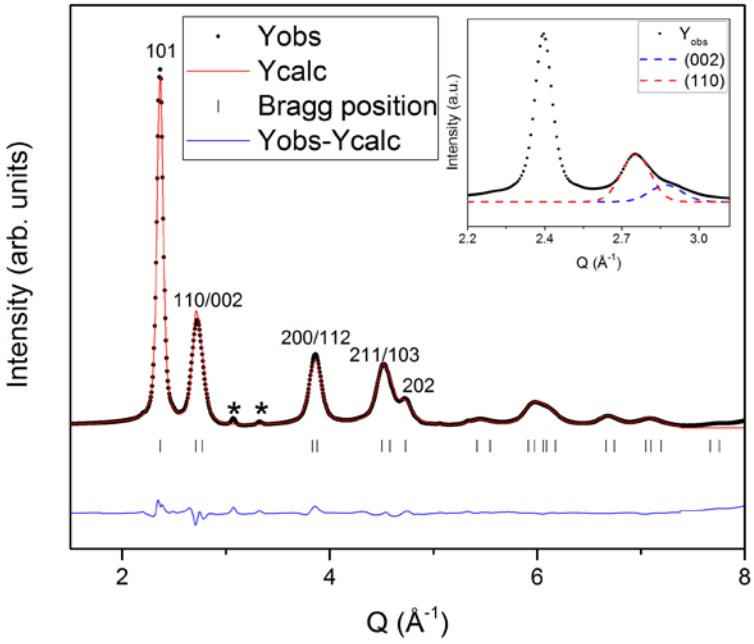

Figure 7. Rietveld refinement of the hydride phase at 500 ºC after 1 absorption - desorption cycle. The split of the (110)/(002) peaks can be seen in the inset, explaining the distorted FCC lattice. The additional peaks are from WC contamination after ball milling and from the Kanthal wire (marked by * in the diffractogram).

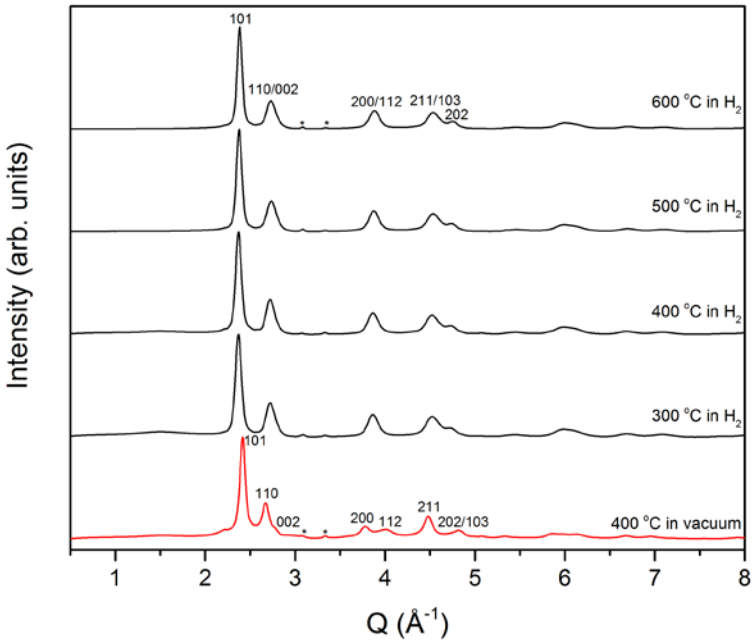

Figure 8. Extracted diffraction patterns of the hydride phase at different temperatures. There are no significant differences between the four samples under hydrogen pressure. However, under vacuum at 400 °C there is a significant decrease of the unit cell volume. The small peaks between Q = 3 and Q = 4 (marked with *) are from the sample environment.

The phase composition was determined using the Rietveld method, which reveal that the material transforms almost completely between the alloy and the hydride phase (figure 9). Furthermore, by extracting the reaction rates using the slope of the quasilinear region of the sigmoidal curves in figure 9, it can be seen that the reaction rate increases with the number of cycles. However, this increase is limited to 20 %, indicating that the effect of activation is not so large in this alloy. The volume of the unit cell also increases with cycling, indicating a higher amount of hydrogen absorbed during cycling. Reaction kinetics of alloy hydrides have previously been observed to depend on both cycle number [26] as well as deformation and strain [27]. Given that high-entropy alloys exhibit a high degree of internal strain due to the lattice distortion [28], a behaviour such as this can be expected as the alloys are strained by themselves and already activated by the lattice distortion.

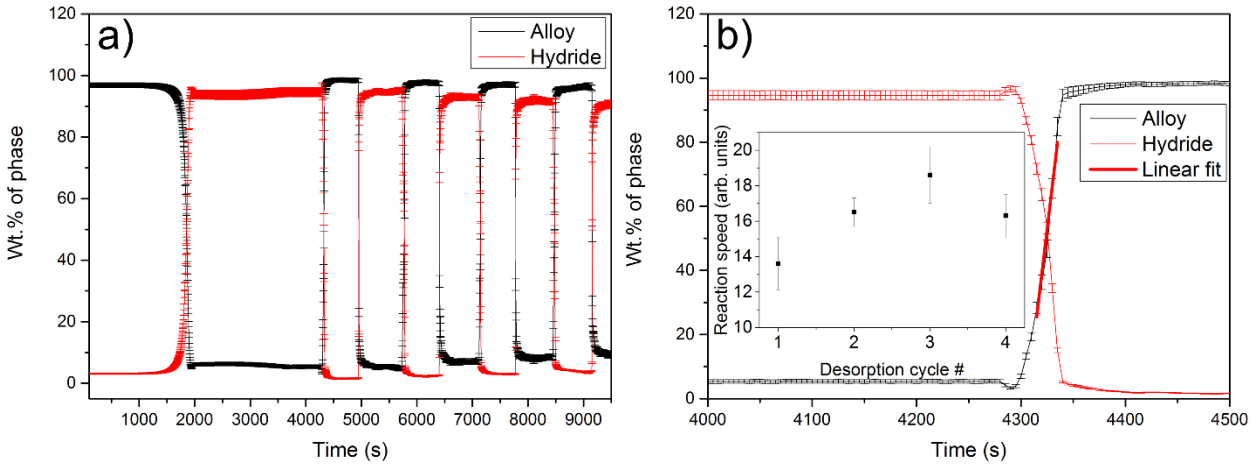

Figure 9. Phase contents for the alloy and hydride phase, extracted from sequential Rietveld refinements of the 500 °C SR-PXD data (a) and determination of the desorption reaction rate from the quasilinear region of the transition (b). The inset shows the reaction rate as function of cycle number.

3.3. Neutron diffraction

In order to determine the positions of the hydrogen (deuterium) atoms in the structure, NPD was utilised. Unfortunately, a combination of the high neutron absorption cross section of the material (especially Hf, 104.1 barn [29]) and the sample environment limits the quality of the *in-situ* NPD data (the measurements were performed *in-situ* under 50 bar H_2(g) at a temperature of 500 °C, which required the samples to be put in a thick walled steel can).

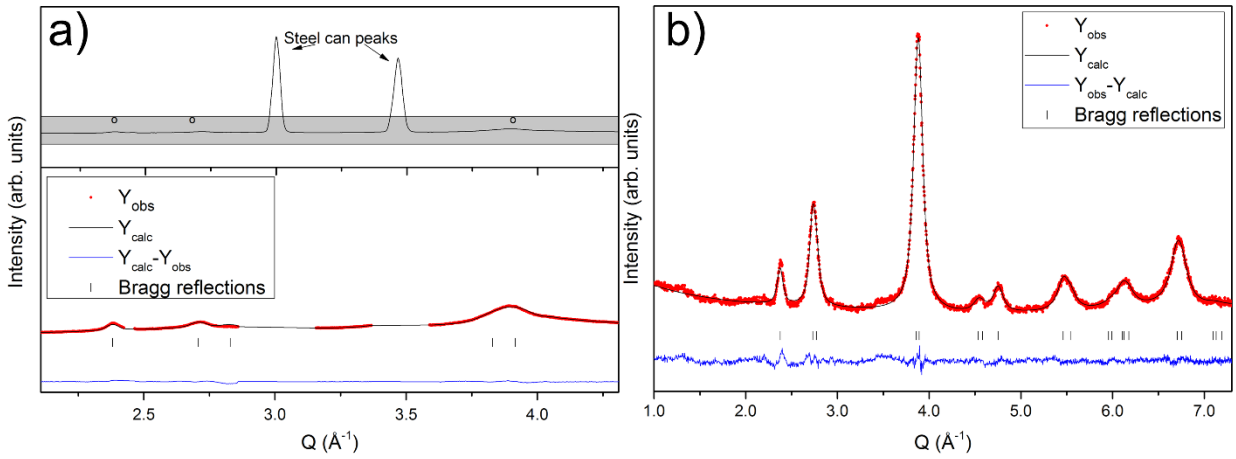

Figure 10. (a) *In-situ* NPD measurement at 500 °C and 50 bar D_2 with the upper pattern showing the total data and the lower pattern showing the relevant area used in the Rietveld refinement (steel can intensities excluded) [30]. The grey area in the upper pattern highlights the area shown in the lower pattern. (b) *Ex-situ* measurement at room temperature after obtaining the deuteride at 500 ºC and 50 bar.

As can be seen in figure 10 a, very limited information can be extracted from the *in-situ* neutron diffraction data recorded at 500 °C. There are only few peaks with detectable intensities observed in the measured range ($0.1 < Q < 4.5$ Å^{-1}) and this limits the amount of parameters that can be refined. Thus, the results presented should be judged as qualitative rather than a complete structure

refinement of the deuteride phase. However, from the refinements it can be concluded that deuterium occupies both the tetrahedral and octahedral interstitial sites. There is a preferred occupation of the tetrahedral sites (as expected) but the difference in occupation is minute (53:47). The similar occupancy level of the tetrahedral and octahedral sites suggests that both interstitial sites are filled at the same time, rather than preferential filling of the tetrahedral sites followed by the octahedral. Furthermore, the refined occupation is significantly lower than expected for the deuteride (H/M ~0.5), something that could possibly be related to the high temperature leading to a much higher equilibrium pressure. Also, the unit cell parameters of the deuteride were determined to be a = 3.276(10) Å and c = 4.451(20) Å, which are significantly different compared to the previously determined values of the hydride at room temperature (a = 3.2183(4) Å, c = 4.6556(16) Å) in ref. [14], but in good agreement with the *in-situ* XRD data presented here. Based on the NPD data, a structure model for the metal deuteride phase at 500 °C, based on a distorted FCC structure where the tetragonal unit cell (figure 11) has one metal site (0, 0, 0) and two independent deuterium sites (tetrahedral: (0, ½, ¼) and (0, ½, ¾), octahedral z-site: (0, 0, ½)) is suggested. The occupancy was set unity on the metal site (20 at.% of each metal) and refined on the deuterium sites yielding the 53:47 ratio.

The *ex-situ* NPD measurement of the deuteride at room temperature (~25 °C) at the PUS instrument (with a deuterium content of D/M = 1.85 by thermogravimetry, deuterated at similar pressures and reaction times as the *in-situ* measurement but measured after cooling to room temperature) shows a different behaviour compared to the *in-situ* measurement. The room temperature data can be fitted well with a tetragonal phase, a = 3.2546(6) Å and c = 4.536(1) Å (figure 10 b). The deuterium occupancy in the tetrahedral and octahedral sites were refined to 92.9(7) % and 5.2(3) %, respectively, corresponding to H/M = 1.91. The data could also be fitted with a cubic fluorite phase, a = 4.5807(6) Å (see SI, figure 1), with a slight increase of R_{wp} to 3.68 %, compared to 3.48 % for the tetragonal model. The increase of symmetry changed the refined D occupancies less than 2 standard deviations. However, this is consistent with a D/M ratio ≈ 2 and a predominant occupation of the tetragonal sites, which is expected to yield a cubic symmetry (see proposed reaction pathway in [14]). Interestingly, the tetragonal distortion seems to depend both on temperature and the H/M (or D/M) ratio. A detailed NPD investigation on the structural transitions of the material is needed to completely elucidate the phase diagram for this HEA-H/D system, but is outside the scope of the current study.

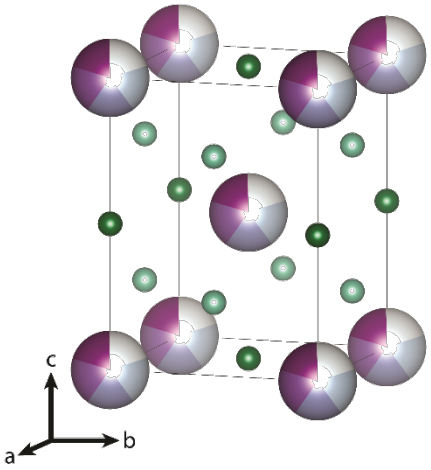

Figure 11. Structural model for the metal deuteride. The metal site is (0, 0, 0) with an occupancy of 20% of each of the 5 individual metal atoms. The deuterium occupies both tetrahedral ((0, ½, ¼) and (0, ½, ¾)) and octahedral (0, 0, ½) sites in the structure.

3.4. Pressure-composition isotherm measurements

To evaluate the total hydrogen storage capacity as well as the thermodynamic parameters of the HEA, isothermal hydrogen absorption measurements were performed. The pressure-composition isotherms (PCI) at 289 and 317 °C (figure 12) show a single plateau at ~0.05 and 0.1 bar, respectively.

By performing the isothermal absorption measurements at several different temperatures, thermodynamic parameters, i.e. the reaction enthalpy and entropy can be extracted using the van't Hoff equation:

$$\ln\left(\frac{P}{P_0}\right) = \frac{\Delta H}{RT} - \frac{\Delta S}{RT}$$

where P_0 is atmospheric pressure, ΔH and ΔS are the changes in enthalpy and entropy, respectively, and R is the gas constant. The results show a reaction enthalpy and entropy of -59 kJ/mol H_2 and 82 J/K mol H_2. The enthalpy value is quite reasonable given that the stability of these hydrides is in between that of the corresponding AB_5- (-32 kJ/mol H_2 [31]) and Mg-hydrides (-74 kJ/mol H_2 [25]).

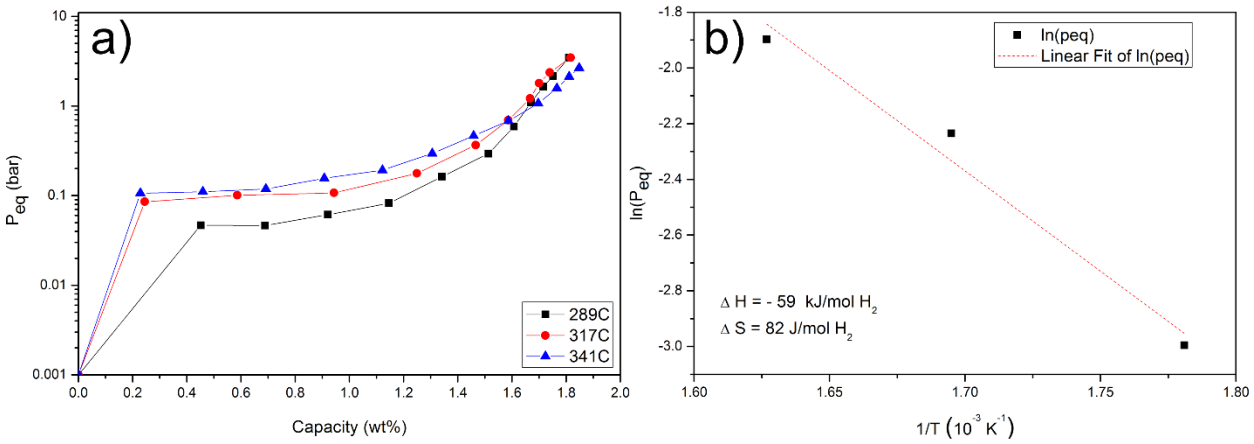

Figure 12. Pressure-Composition Isotherms for hydrogen absorption in HfNbTiVZr at 289, 317 and 341 °C (a) and van't hoff plot using the plateau pressure from the PCI:s (b).

The maximum capacity measured is 1.9 H/M at 10 bar, irrespective of temperature. This value is in good agreement with our previous PCI measured at 299 °C reported in [14]. The outstanding hydrogen storage capacity of 2.5 H/M was obtained at higher pressure, around 50 bar.

4. Summary and conclusions

The hydrogenation mechanism of the high-entropy alloy, HfNbTiVZr, under different pressure-temperature conditions have been investigated. The alloy can absorb large amounts of hydrogen by a phase transition from the BCC metal phase to a BCT hydride phase, reaching an H/M ratio of at least 2.5. A full hydrogen desorption requires a temperature of 500 ^{o}C in vacuum. By neutron diffraction, the hydrogen was determined to occupy both the tetrahedral and octahedral interstitial sites in the tetragonal structure at high temperature and pressure (500 °C, 50 bar D_2). However, room temperature data could be fitted with both the tetragonal phase and a cubic phase (CaF_2-type structure) with D primarily in the tetragonal positions. A more detailed study of the role of hydrogen during structural transitions is needed to fully elucidate the alloy-hydride phase diagram. The reaction rate only increases slightly (~20%) with the amount of cycles, indicating a low activation energy for this alloy. The microstructure also changes with hydrogen sorption experiments as the alloy decrepitates when as subjected to a hydrogen environment.

From reviewing all the experimental results, it is clear that hydrogen storage in the HfNbTiVZr equimolar high-entropy alloy shows great prospects. The storage is reversible at 500 ^{o}C and the internal strain seems to facilitate hydrogen occupation in unexpected interstitial positions. The structural information that can be extracted from *in-situ* neutron diffraction at high temperatures is limited but clearly indicates occupancy of both tetrahedral and octahedral interstitial sites, which can explain the very high hydrogen storage capacity.

5. Supporting Information Available

Table 1: Chemical composition from EDS.

Figure 1: Ex-situ neutron diffraction and refinement using a FCC phase.

6. Acknowledgements

Financial support from the Swedish Foundation for Strategic Research, project “SSF – Development of processes and Materials in AM”, as well as Nordforsk, project “Neutrons for multi-functional hydrides - FunHy” is gratefully acknowledged. Parts of this research were carried out at the light source PETRA III (beamline P02.1) at DESY, a member of the Helmholtz Association (HFG). The authors also thank Dr. Premysl Beran for valuable scientific discussions. KTM, MP and TRJ acknowledges the support from the Danish National Research Foundation, Center for Materials Crystallography (DNRF93), the Innovation Fund Denmark (HyFillFast), the Danish Research Council for Nature and Universe (Danscatt), and the Carlsberg Foundation.

7. References

1. Sakintuna, B.; Lamari-Darkrim, F.; Hirscher, M. Metal hydride materials for solid hydrogen storage: A review. *Int. J. Hydrogen Energy* **2007,** 32, 1121-1140.
2. Yeh, J. W.; Chen, S. K.; Lin, S. J.; Gan, J. Y.; Chin, T. S.; Shun, T. T.; Tsau, C. H.; Chang, S. Y. Nanostructured High-Entropy Alloys with Multiple Principal Elements: Novel Alloy Design Concepts and Outcomes. *Adv. Eng. Mater.* **2004,** 6, 299-303.
3. He, F.; Wang, Z.; Li, Y.; Wu, Q.; Li, J.; Wang, J.; Liu, C. T. Kinetic ways of tailoring phases in high entropy alloys. *Sci. Rep.* **2016,** 6, 34628.
4. Yurchenko, N.; Stepanov, N.; Salishchev, G. Laves-phase formation criterion for high-entropy alloys. *Mater. Sci. Technol.* **2016,** 33, 17-22.
5. Senkov, O. N.; Wilks, G. B.; Scott, J. M.; Miracle, D. B. Mechanical properties of Nb25Mo25Ta25W25 and V20Nb20Mo20Ta20W20 refractory high entropy alloys. *Intermetallics* **2011,** 19, 698-706.
6. Gludovatz, B.; Hohenwarter, A.; Catoor, D.; Chang, E. H.; George, E. P.; Ritchie, R. O. A fracture-resistant high-entropy alloy for cryogenic applications. *Science* **2014,** 345, 1153-8.
7. Lu, Y.; Dong, Y.; Guo, S.; Jiang, L.; Kang, H.; Wang, T.; Wen, B.; Wang, Z.; Jie, J.; Cao, Z.; Ruan, H.; Li, T. A promising new class of high-temperature alloys: eutectic high-entropy alloys. *Sci. Rep.* **2014,** 4, 6200.
8. Lu, Y.; Gao, X.; Jiang, L.; Chen, Z.; Wang, T.; Jie, J.; Kang, H.; Zhang, Y.; Guo, S.; Ruan, H. Directly cast bulk eutectic and near-eutectic high entropy alloys with balanced strength and ductility in a wide temperature range. *Acta mater.* **2017,** 124, 143-150.
9. Shafeie, S.; Guo, S.; Hu, Q.; Fahlquist, H.; Erhart, P.; Palmqvist, A. High-entropy alloys as high-temperature thermoelectric materials. *J. Appl. Phys. (Melville, NY, U. S.)* **2015,** 118, 184905.
10. Borkar, T.; Chaudhary, V.; Gwalani, B.; Choudhuri, D.; Mikler, C. V.; Soni, V.; Alam, T.; Ramanujan, R. V.; Banerjee, R. A Combinatorial Approach for Assessing the Magnetic Properties of High Entropy Alloys: Role of Cr in AlCoxCr1–xFeNi *Adv. Eng. Mater.* **2017,** 19, 1700048.
11. Kunce, I.; Polanski, M.; Bystrzycki, J. Structure and hydrogen storage properties of a high entropy ZrTiVCrFeNi alloy synthesized using Laser Engineered Net Shaping (LENS). *Int. J. Hydrogen Energy* **2013,** 38, 12180-12189.
12. Kunce, I.; Polanski, M.; Bystrzycki, J. Microstructure and hydrogen storage properties of a TiZrNbMoV high entropy alloy synthesized using Laser Engineered Net Shaping (LENS). *Int. J. Hydrogen Energy* **2014,** 39, 9904-9910.
13. Kunce, I.; Polański, M.; Czujko, T. Microstructures and hydrogen storage properties of La Ni Fe V Mn alloys. *Int. J. Hydrogen Energy* **2017,** 42, 27154-27164.
14. Sahlberg, M.; Karlsson, D.; Zlotea, C.; Jansson, U. Superior hydrogen storage in high entropy alloys. *Sci. Rep.* **2016,** 6, 36770.
15. Hansen, B. R. S.; Moller, K. T.; Paskevicius, M.; Dippel, A. C.; Walter, P.; Webb, C. J.; Pistidda, C.; Bergemann, N.; Dornheim, M.; Klassen, T.; Jorgensen, J. E.; Jensen, T. R. In situ X-ray diffraction environments for high-pressure reactions. *J. Appl. Crystallogr.* **2015,** 48, 1234-1241.
16. Hammersley, A. P.; Svensson, S. O.; Hanfland, M.; Fitch, A. N.; Hausermann, D. Two-dimensional detector software: From real detector to idealised image or two-theta scan. *High Pressure Res.* **1996,** 14, 235-248.

17. Rietveld, H. M. A Profile Refinement Method for Nuclear and Magnetic Structures. *J. Appl. Crystallogr.* **1969,** 2, 65.
18. Rodríguez-Carvajal, J. Recent advances in magnetic structure determination by neutron powder diffraction. *Phys. B* **1993,** 192, 55-69.
19. Hauback, B. C.; Fjellvåg, H.; Steinsvoll, O.; Johansson, K.; Buset, O. T.; Jørgensen, J. The high resolution Powder Neutron Diffractometer PUS at the JEEP II reactor at Kjeller in Norway. *J. Neutron Res.* **2000,** 8, 215-232.
20. Niwa, M.; Shikama, T.; Yonezu, A. Mechanism of hydrogen embrittlement cracking produced by residual stress from indentation impression. *Mater. Sci. Eng., A* **2015,** 624, 52-61.
21. Akiba, E.; Nakamura, Y. Hydrogenation properties and crystal structures of Ti−Mn-V BCC solid solution alloys. *Met. Mater. Int.* **2001,** 7, 165-168.
22. Knappe, P.; Müller, H.; Mayer, H. W. Tetragonal rare earth hydrides REH(D)≈2.33 (RE ☐La, Ce, Pr, Nd, Sm) and a neutron diffraction study of NdD2.36. *J. Less-Common Met.* **1983,** 95, 323-333.
23. Møller, K. T.; Hansen, B. R. S.; Dippel, A.-C.; Jørgensen, J.-E.; Jensen, T. R. Characterization of Gas-Solid Reactions using In Situ Powder X-ray Diffraction. *Z. Anorg. Allg. Chem.* **2014,** 640, 3029-3043.
24. Peisl, H. In *Hydrogen in Metals I, Top. Appl. Phys*; Völkl, G. A. a. J., Ed.; 1978; Vol. 28, p 53.
25. Fukai, Y. *The Metal-Hydrogen System*. 2nd rev. and updat;2. Aufl.;2;2nd;2nd; ed.; Springer: New York;Berlin;, 2005, 21.
26. Korablov, D.; Angstrom, J.; Ley, M. B.; Sahlberg, M.; Besenbacher, F.; Jensen, T. R. Activation effects during hydrogen release and uptake of MgH2. *Int. J. Hydrogen Energy* **2014,** 39, 9888-9892.
27. Dufour, J.; Huot, J. Rapid activation, enhanced hydrogen sorption kinetics and air resistance in laminated Mg–Pd 2.5at.%. *J. Alloys Compd.* **2007,** 439, L5-L7.
28. Miracle, D. B.; Senkov, O. N. A critical review of high entropy alloys and related concepts. *Acta Mater.* **2017,** 122, 448-511.
29. Sears, V. F. Neutron scattering lengths and cross sections. *Neutron News* **1992,** 3, 26-37.
30. Sahlberg, M.; Cedervall, J.; Hansen, T.; Ulf, J.; Karlsson, D., In-Situ Neutron Diffraction and Phase Transformation of an Hydride Forming High-Entropy Alloy. In Institut Laue-Langevin (ILL): 2017.
31. Lundin, C. E.; Lynch, F. E. Solid state hydrogen storage materials for application to energy needs, Air Force Off. Sci. Res., [Tech. Rep.] AFOSR-TR (U. S.). 1976.

For Table of Contents Only

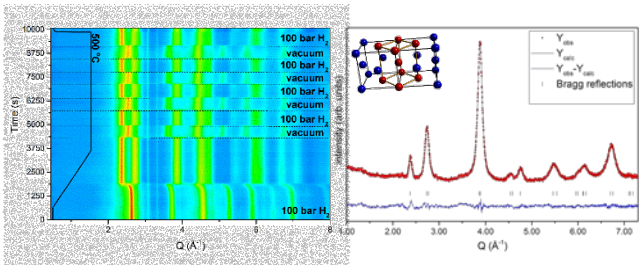

Phase transformations in a hydride forming high-entropy alloy (HEA) of HfNbTiVZr was characterised by *ex-situ* and *in-situ* synchrotron radiation X-ray and neutron diffraction. The BCC alloy undergo a phase transformation to a BCT structure upon hydrogenation. The alloy is stable during hydrogen cycling at 500 ^{o}C. Hydrogen occupies both tetrahedral and octahedral interstitial sites. The HEA has potential as hydrogen storage materials.